EUROPEAN FUSION DEVELOPMENT AGREEMENT

EFDA–JET–PR(03)52

T. Onjun, V. Parail, G. Bateman, A.H. Kritz, J. Lönnroth, G. Huysmans,
and JET EFDA contributors

Integrated Pedestal and Core Modeling of JET Triangularity Scan Discharges

Integrated Pedestal and Core Modeling of JET Triangularity Scan Discharges

T. Onjun[1], V. Parail[4], G. Bateman[1], A.H. Kritz[1], J. Lönnroth[3], G. Huysmans[2], and JET EFDA contributors*

[1]Lehigh University Physics Department, 16 Memorial Drive East, Bethlehem, PA 18015
[2]Association EURATOM-CEA, CEA Cadarache, DRFC, Batiment 513, 13108 Saint-Paul-Lez-Durance, France
[3]Association EURATOM-Tekes, Helsinki University of Technology, P.O. Box 2200, 02015 HUT, Finland
[4]EURATOM/UKAEA Fusion Association, Culham Science Centre, Abingdon Oxon OX14 3DB, UK
** See annex of J. Pamela et al, "Overview of Recent JET Results and Future Perspectives", Fusion Energy 2000 (Proc. 18th Int. Conf. Sorrento, 2000), IAEA, Vienna (2001).*

Preprint of Paper to be submitted for publication in
Physics of Plasmas

ABSTRACT.
Simulations of four JET type I ELMy H-mode discharges in a triangularity scan are carried out using the JETTO integrated modeling code with a predictive core and pedestal model that includes the effect of ELMs. The pedestal width is calculated using a theory-motivated model based on magnetic and flow shear stabilization and the pressure gradient is limited by MHD ballooning instability. The Mixed Bohm/gyro-Bohm anomalous transport model is used in the plasma core while ion thermal neoclassical transport is used in the pedestal. It is found that the predicted plasma profiles reproduce the observed plasma profiles. An MHD stability analysis is carried out for the discharges in the triangularity scan using HELENA and MISHKA codes, which include infinite-*n* ideal ballooning, finite-*n* ballooning, and low-*n* kink/peeling modes. It is found that higher triangularity plasmas have easier access to the second region of ballooning mode stability, which allows the edge pressure gradient to increase to higher levels.

1. INTRODUCTION

Predictive integrated modeling codes, such as the JETTO code [1] and the BALDUR code [2], are used to predict the time evolution of the temperature, density and plasma current profiles in tokamaks. Many of the simulations that have been carried out with these codes predict the core plasma profiles using boundary conditions taken from experimental data [3, 4]. For H-mode simulations, the boundary conditions have generally been taken from experimental values at the top of the pedestal [4]. The pedestal is a narrow region located near the separatrix, typically occupying less than 5% of the plasma minor radius. The height of the pedestal has a strong influence on the performance of H-mode plasmas due to the stiffness of the core transport [5, 6, 7, 8]. For future experiments, such as ITER [9] and FIRE [10], where pedestal data is not available, it is important to have a reliable methodology for predicting the boundary conditions [11].

Several approaches have been developed to compute the boundary conditions that can be used in predictive integrated modeling codes [12, 13, 14]. One approach is to assume that the pressure gradient is uniform within the steep gradient region of the pedestal [13]. The temperature at the top of the pedestal, $T_{ped,}$ is then expressed in terms of the pedestal density, n_{ped}, the pressure gradient within the pedestal, $\partial p/\partial r$, and the pedestal width, Δ. The notation used in this paper is described in Table I. It is assumed that pressure gradient within the pedestal is limited by the ideal ballooning stability, where the critical pressure gradient of ballooning mode instability is estimated using a simple analytical model for the critical normalized pressure gradient. The RMS errors that were obtained in Ref. [13] indicate that the plasma processes near the separatrix are ps;bably more complicated than those used in the simple model and a somewhat more sophisticated approach is required than the one used in Ref. [13].

A more advanced approach described in this paper for the pedestal has been developed and used in the integrated predictive modeling code JETTO. This approach allows for a self-consistent calculation of the plasma equilibrium and transport, which takes into account the evolution of the

edge pressure gradient and the edge current density. Both the edge pressure gradient and the edge current density have a strong influence on stability of the ballooning modes. In particular, a strong pressure gradient leads to a strong edge current density, which can possibly result in access to the second stability region of ballooning modes in the s-α plane. In the JETTO code, it is assumed that the edge pressure gradient is limited by the ballooning instability. The JETTO code is linked with ideal MHD stability codes, HELENA and MISHKA, to evaluate the critical pressure gradient limit, α_c. The HELENA code is used to evaluate plasma stability against infinite-n ideal ballooning modes at the time before each ELM crash. In addition, the stability criterion used in the JETTO code is veried using the MISHKA MHD stability analysis code to determine the stability of infinite-*n* ballooning and low-*n* kink/peeling modes, which play an important role in limiting the pressure gradient. If the HELENA and MISHKA analysis indicates a normalized pressure gradient greater than the value of α_c used in the JETTO simulation, the value of α_c used in JETTO code is then increased, and the simulation is repeated. The process continues until the value of α_c used in the JETTO simulation is consistent with the maximum pressure gradient indicated by the HELENA and MISHKA stability codes.

In the simulations of the JET discharges that are presented in this paper, edge boundary conditions are imposed at the separatrix and a predictive pedestal model is used together with a core transport model in the JETTO code. One assumption made about the pedestal physics is that the turbulent transport is completely suppressed in the region between the top of the pedestal and the separatrix. All the diagonal elements of the transport matrix within the pedestal are taken to be the ion neoclassical thermal conductivity, calculated at the top of the pedestal using the NCLASS module [15]. This assumption implicitly implies that electron transport is still anomalous and is supported by recent studies of short wave length turbulence associated with the electron temperature gradient mode [16]. The assumption regarding the uniformity of neoclassical transport within the barrier is merely a reflection of the fact that the pedestal width is usually of the order of the ion orbit width (or banana width), which implies limited variation of the neoclassical transport across the edge transport barrier. The reduction of transport within the pedestal region results in a sharp pressure gradient and an associated bootstrap current, computed using the NCLASS model, that builds up within the pedestal region. Another assumption regarding the pedestal model is that the pedestal width is given by a pedestal model based on magnetic and flow shear stabilization [12, 13].

The organization in this paper is as follows. The details of the four discharges considered in this paper are described in Section II, together with some other relevant experimental data. The description of the pedestal width model is presented in Section III. The details of the integrated transport code JETTO and of the transport model are presented in Section IV. Simulation results and a discussion of these simulations are given in Section V. MHD stability analysis of the simulated profiles are described in Section VI, followed by conclusions in Section VII.

2. EXPERIMENTAL DATA

Predictive simulations using the JETTO code are carried out for 4 JET discharges that have similar

plasma current, magnetic field and elongation, but have different triangularity [17]. The pulse numbers for these four discharges are 53186, 53187, 53298 and 52308. The plasma current, I_p, is fixed at 2.5MA while the toroidal magneticeld, B_T, is in the limited range from 2.6 to 2.7T. The elongation at the separatrix is approximately 1.7 and the triangularity at the separatrix ranges from 0.25 to 0.49. More details about these discharges are shown in Table. II.

These four discharges are all quasi-stationary type I ELMy H-mode plasmas. Figure 1 shows the time history of the D_α signal measured at the edge of the plasma and Fig. 2 shows the stored energy and the heating power for each of the discharges. The stored energy for discharges 53186 and 53187 is roughly constant during the period from 20.5 sec to 25.5sec. For discharge 53298, the stored energy is constant during the period from 17.0 sec to 23.5sec, and for discharge 52308, the stored energy is constant from 17.0sec to 19.5sec. Note that the stored energy is approximately the same in all of the discharges during the quasi-stationary period, and the confinement time is consistent with the H-mode scaling $\tau_{E,th}^{IPB98(y;2)}$ [18]. High resolution Rogowskii coils are used to measure the time evolution of the diamagnetic energy. Figure 3 shows the variation in the stored plasma energy between two consecutive type I ELMs for JET discharge 53298, together with the D_α signal. It can be seen that the total plasma stored energy decreases about 10% during an ELM crash. Also, the characteristic ELM frequency is approximately 17Hz.

The experimental pressure profiles used in the comparisons presented in this paper were taken from the core LIDAR Thomson scattering measurement and from the Charge Exchange (CX) spectroscopy. Note that the LIDAR and CX diagnostics do not have sufficient resolution near the edge of the plasma to resolve the width of the pedestal. As a result, it is difficult to compute the exact width of the pedestal from the experimental data. Instead, in this work, measurements at the top of the pedestal with these diagnostics were used as a way to compare experimental results with the results obtained in the simulations. In Fig.4, the experimental and simulated pressure profiles are plotted for all four discharges. The smoothed experimental data curves are obtained by mapping the raw experimental data onto the JETTO computational grid using a spline routine.

3. THE PEDESTAL WIDTH MODEL BASED ON MAGNETIC AND FLOW SHEAR STABILIZATION

The fundamental physics associated with this pedestal width is that the turbulence within the pedestal is suppressed by the $\mathbf{E_r \times B}$ flow shear. The pedestal is formed in the region where the stabilizing $\mathbf{E_r \times B}$ shearing rate, $\boldsymbol{\gamma_{Er \times B}}$, exceeds the turbulence growth rate, γ_s, so that the stabilization condition can be written as

$$\boldsymbol{\gamma_{Er \times B} \geq \gamma_s} \tag{1}$$

Within the pedestal of well-developed H-mode plasmas, it is assumed, see for example Ref. [12], that the radial electriceld, Er, is determined by the pressure gradient, $\partial p/\partial r$;

$$neE_r = \frac{\partial p}{\partial r} \tag{2}$$

where n is the plasma density and e is the electron charge. This results in an $\mathbf{E_r \times B}$ drift velocity given by

$$v_{Er \times B} = \frac{E_r}{B_T} = \frac{1}{neB_T}\frac{\partial p}{\partial r} \approx \frac{1}{neB_T}\frac{p}{\Delta} = \frac{\rho_i c_s}{\Delta} \tag{3}$$

where Δ is the width of the pedestal, ρ_i is the ion gyro radius and c_s is the ion sound velocity. As a result, the $\mathbf{E_r \times B}$ shearing rate, $\boldsymbol{\gamma_{Er \times B}}$, can be approximated as

$$\gamma_{Er \times B} = \frac{\partial v_{Er \times B}}{\partial r} \approx \frac{\rho_i c_s}{\Delta^2}. \tag{4}$$

An estimate for the growth rate for the turbulence due to drift modes, taking into account of the reduction associated with the magnetic shear in the pedestal region [12], is given by

$$\gamma_s \propto \frac{c_s}{\Delta}\frac{1}{s^2}. \tag{5}$$

where s is the magnetic shear. The scaling of the pedestal width is obtained by substituting Eqs. 4 and 5 into Eq. 1 and solving for Δ. The resulting pedestal width is given by

$$\Delta \propto \rho_i s^2. \tag{6}$$

The constant of proportionality in Eq. 6 is found to be 2.42 where the magnetic shear, s, is calculated using the shear prescription described in Ref. [13]. Note that the calculation of the magnetic shear, s, involves a non-linear iteration, and the constant of proportionality in Eq. 6 was chosen to minimize the RMS deviation between predicted pedestal temperatures based on the width scaling described above and the corresponding experimental pedestal temperatures for 533 data points. Further details can be found in Ref. [13].

4. THE INTEGRATED PREDICTIVE TRANSPORT CODE JETTO

The $1^1/_2$D transport code JETTO is used to simulate the time evolution of plasma profiles such as current density, temperatures and particle densities in both the core and pedestal regions. The edge boundary conditions, such as the electron and ion temperature, are imposed at the separatrix in the JETTO code. The electron and ion temperature at the separatrix is taken to be 200eV while the electron density at the separatrix is assumed to be $2\times10^{19}m^{-3}$. It was shown in Ref. [19] that for type I ELMy H-mode plasma without strong gas puffing, the modeling results are not sensitive to the choice of boundary conditions at the separatrix. Two main assumptions are made in the modeling

of the pedestal: The first assumption is about the transport within the edge barrier, both between ELMs and during ELMs, and the second assumption is related to the scaling of the width of the pedestal, which was discussed in the previous section.

As noted in Section I, it is assumed that anomalous transport is suppressed within the edge transport barrier between ELMs. For the anomalous transport in the core plasma, the Mixed Bohm/ gyro-Bohm model [20] is used. The reduction in the transport coefficients within the pedestal results in the development of a steep pressure gradient in the pedestal region, which causes an increase in the bootstrap current density within the pedestal. The steep edge pressure gradient and the resulting edge current density eventually lead to destabilization of either a ballooning mode [21, 22] or a peeling mode [23, 24, 25, 26]. The destabilization of these modes then triggers an ELM crash, which results in a loss of plasma energy as well as the particles to the wall. The effect of the removal of the plasma energy and particles associated with ELMs is included in these JETTO simulations, as described below. The computed normalized pressure gradient, $[\alpha \equiv -(a_0 \mu q^2/\in B_T)(\partial p/\partial \rho)]$, is compared with the prescribed critical normalized pressure gradient, α_c, above which the plasma is considered to be unstable with respect to the ballooning instability. When the value of α anywhere inside the pedestal region exceeds the value of α_c, all diagonal transport coefficients in the JETTO code are temporarily increased by a factor of $A_{particle;\ thermal}$ above the ion neoclassical transport level within the pedestal for a specified time interval τ_{ELM} = 0.4ms, which is of the order of a typical ELM duration in JET type I ELMy H-mode discharges (see Fig.3). The details of the increase in the transport during an ELM crash are as follows: The increases occurs linearly during the first quarter of the duration of the ELM, that is during $\Delta t = \tau_{ELM}/4$. The transport remains at this maximum level during one half of the ELM crash time interval. Finally, the transport decreases linearly back to the neoclassical level during the final quarter of the ELM crash time interval. The factor for the increase in particle transport during an ELM crash is 100 ($A_{particle}$ = 100). The thermal transport during the ELM is taken to be 300 times that of the ion neoclassical thermal transport at the top of the pedestal ($A_{thermal}$ = 300). The rapid increase in the transport coefficients within the pedestal results in a pulse of particles and energy leaving the plasma. This burst of particles and energy depletes the plasma edge and returns the system to an MHD-stable state α with less than α_c. This cycle of edge instability, which represents the ELM activity, repeats throughout the simulation. Note that the width of an ELM crash in the simulation is approximately the width of the pedestal.

The ELM transport model, described above, has a number of ad hoc parameters that determine both ELM amplitude and its repetition rate. This model, which has been comprehensively tested against a wide range of JET data (see, for example in Refs. [27, 28]), leads to the following conclusions: The ELM amplitude (taken as the ratio of the energy loss during the ELM to the average plasma energy) scales linearly with the parameter $H_{particle;\ thermal} \propto A_{particle;\ thermal}\ \tau_{ELM}$ and the ELM frequency scales inversely proportional to H. Both the ELM amplitude and its duration are controlled by non-linear MHD phenomena. The values of $A_{particle;\ thermal}$ and τ_{ELM} are adjusted in order to bring the modeling results into closer agreement with experimental data since the model

for ELMs are not fully developed. It is found that the time averaged total plasma energy content does not depend sensitively on the parameter $H_{particle;\,thermal}$. Instead, the thermal energy confinement time is almost entirely controlled by the core transport (which in turn depends on plasma parameters at the top of the barrier as a result of the profile stiffness associated with core transport).

5. JETTO SIMULATION RESULTS

The simulations of 4 JET discharges (see discharge parameters in Table II) are carried out using the JETTO code during the quasi-stationary period of the H-mode phase of the discharge (see Fig.2) in order to avoid the influence of initial conditions such as the current density profile redistribution. The anomalous transport in the core is calculated using the Mixed Bohm/gyro-Bohm transport model [20], which has been tested in simulations of a variety of discharges with different plasma conditions in different tokamaks. For example, the results of simulations using the Mixed Bohm/gyro-Bohm transport model yield agreement with experimental data within 15% normalized RMS deviation for L-mode and H-mode plasmas [3, 4]. For simplicity, the effects of sawtooth oscillations have not been included in the simulations shown in this work. This simplication can lead to an overestimation of central plasma pressure, although it should be noted that sawteeth were quite benign in these shots, with a mixing radius not exceeding 20% of the plasma radius. The width of the pedestal is calculated using the pedestal model, which is $\Delta = 2.42\rho_i s^2$. The bases of this pedestal width model were briefly discussed in previous section. Note that the value of magnetic shear, s, for the pedestal width is calculated using the prescription that involves a non-linear iteration, described in Ref. [13].

Figure 4 shows the comparison between the experimental pressure profiles and the predicted pressure profiles at a time just before an ELM crash for discharges 53186, 53187, 53298 and 52308, using the Mixed Bohm/gyro-Bohm for the core and the ion neoclassical transport within the edge barrier, where the pedestal width is given by the model. The over-prediction in the core profiles is probably caused by the absence of sawtooth oscillations, which periodically reduce the central profile of the core profiles. However, it is worth noting that the over-prediction in the pressure profiles near the center of the plasma does not signicantly affect the overall connement, because of the small volume occupied by the central part of the plasma.

It is also found that the average pedestal width prior to an ELM crash in the simulations for the JET triangularity scan in Fig.4 ranges from 3.9cm to 4.4cm, which is about 5% of the minor radius. Unfortunately, there is not enough radial resolution in the edge profile measurements to do a direct comparison between the pedestal width given by the model and experimental data.

In Fig.5, the ion temperature, electron density and ion diffusivity at the top of the pedestal is plotted as a function of time for a simulation of the high triangularity discharge 53298. Note that peaks in ion diffusivity can be used as a signature of the ELM crashes in the JETTO simulations. It can be seen that during each ELM crash (indicated by a high value of the ion diffusivity), both temperature and density at the top of the pedestal decrease dramatically, and then recover after an ELM crash. In the simulation for the JET high triangularity discharge 53298, the ELM frequency is

found to be about 16.5Hz, which is close to the experimental ELM frequency observed in the D_α signal for discharge 53298 shown in Fig.3, approximately 17Hz.

In Fig.6, the simulated $H_{H98(y;2)}$ factor and the stored thermal plasma energy are plotted as a function of time for the JET discharge 53298. The $H_{H98(y;2)}$ factor is dened as $H_{H98(y;2)} \equiv \tau_{E,th}/\tau^{r}_{E}$ where $\tau_{e.th}$ is the thermal energy confinement time. It is found that the average $H_{H98(y;2)}$ factor in the simulations is approximately 1.0 during the interval from 21.0 sec to 22.0 sec. The values of the $H_{H98(y;2)}$ factor are consistent with the experimental values obtained in the JET discharges ($H_{H98(y;2)}$ 1.0). It can also be seen from Fig.6 that the decrease in the simulated thermal energy due to each ELM crash is about 10% of the plasma thermal stored energy before the crash, which is approximately the same as that observed in the experimental data, which is shown in Fig.3.

Figure7 shows the predicted plasma current density profile (J_z) and the simulated bootstrap current density profile (J_{bs}) in each discharge, at a time just before an ELM crash. It can be seen that the bootstrap current density is dominant at the edge of the plasma. The maximum peak of the bootstrap current density is located around 98% flux surface in each of the four discharges. The maximum peak value of the bootstrap current density is the highest in discharge 52308, which is the discharge with the highest triangularity, and the maximum peak of the bootstrap current density is the lowest in discharge 53186, which is the discharge with the lowest triangularity. The increase in the the maximum peak of the bootstrap current density with triangularity results from the increases in the value of the critical normalized pressure gradient, α_c, used in each simulation. Note that the value of α_c is initially arbitrary chosen in each simulation. The stability analysis is then carried for that simulation using the HELENA and MISHKA stability codes. Then, the value of α_c is adjusted so that it agrees with the maximum possible pressure gradient allowed by the stability analysis. This procedure is carried out until the JETTO result is self-consistent with the stability analysis of the HELENA and MISHKA codes. In accordance with neoclassical theory, the bootstrap current density is approximately proportional to the pressure gradient and varies inversely with the collisionality. Since the bootstrap current density appears predominantly in the strong pressure gradient region of the pedestal, it follows that the two driving forces for MHD instabilities, the pressure gradient and the edge current, are coupled. This complex system requires a more sophisticated stability analysis. Such an analysis is carried out and is discussed in the next section.

6. STABILITY ANALYSIS

In order to check the validity ofthe analytical ballooning stability criterion used in the JETTO code, the code is linked with the HELENA and MISHKA MHD stability analysis codes. The HELENA code takes the self-consistent equilibrium produced by the JETTO code, that is the pressure gradient and the current density profiles, together with the corresponding magnetic configuration, at a time just before an ELM crash occurs. The HELENA code then refines the equilibrium in order to provide the resolution required for the stability analysis. This refined equilibrium is used in the HELENA code to generate a ballooning stability s-α diagram. Furthermore, the MISHKA code is

used to evaluate the stability criteria for finite-n ballooning and low-n kink/peeling modes. In this study, the stability analysis is carried out in MISKHA for toroidal mode numbers in the range of n = 1 to n = 14. Note, the version of the MISHKA code employed in this paper is based on the ideal MHD model without dissipation or flow shear.

Stability analyses are carried out with the HELENA and MISHKA codes to evaluate the edge stability at the time just before an ELM crash. Figures 8, 9, 10 and 11 show the stability s-α diagram for the discharges 53186, 53187, 53298 and 52308, respectively. In each figure, the stability s-α diagrams are plotted for the 93%, 94%, 95% and 96% flux surfaces. In each plot, the circle symbol represents the location of the operational point for the pressure gradient at that flux surface. The region of instability associated with the infinite-*n* ideal ballooning modes is indicated with crosses and the numbers indicate the most unstable mode of finite-*n* ballooning and low-*n* kink/peeling modes at each location on the s-α plane. Note that only unstable modes with the growth rates greater than 0.03 of the Alfvén frequency are included in Figs 8, 9, 10 and 11. A weakly unstable mode might be stabilized if finite Larmor radius or ion diamagnetic drift effects were included. A discussion of this stabilizing effect is beyond the scope of this study.

Figure 8 shows the stability s- diagram for the low triangularity JET discharge 53186 (δ = 0.25). It can be seen that the edge pressure gradient is limited by an n = 2 toroidal mode. It is also found that there is no access to the second stability region of ballooning modes, since the access is closed by finite-n ballooning and low-n kink/peeling modes. The normalized pressure gradient at the 95% flux surface for this simulation is approximately 3.7.

The stability s-α diagram for the slightly higher triangularity JET discharge 53187 (δ = 0.32) is shown in Fig.9. It can be seen that the edge pressure gradient is limited by an n = 3 toroidal mode. There is a limited access to second stability region of ballooning modes. The normalized pressure gradient at the 95% flux surface for this simulation is approximately 5.3. It can be seen that the pressure gradient at the 95% flux surface increases by 43% above the value of the low triangularity discharge 53186 (∂ = 0.25).

Figure 10 shows the stability s-∝ diagram for the higher triangularity JET Pulse No: 53298 (δ = 0.45). It can be seen that there is a wide access to the second stability region of ballooning modes. The edge pressure gradient appears to be limited by an *n* = 2 toroidal mode, but very close to the finite *n* = 10 ballooning mode as well. The normalized pressure gradient at the 95% flux surface obtained in this simulation is approximately the same as that obtained in the simulation for the δ = 0.32 plasma.

Finally, the stability diagram from the MISKHA code produced for the highest triangularity discharge 52308 (δ = 0.49) is shown in Fig. 11. It can be seen that that there is access to the second stability region of ballooning modes for this simulation. The access to second stability of the edge pressure gradient is limited by thenite *n* = 14 ballooning mode. The normalized pressure gradient at the 95% flux surface for this simulation is approximately 6.2. Thus, when δ = 0.49, the normalized pressure gradient at 95% flux surface is 68% higher than the value obtained in the simulation of the δ = 0.25 low triangularity discharge.

CONCLUSION

Simulations of four JET type I ELMy H-mode discharges in a triangularity scan are carried out using the integrated modeling code JETTO. In all of these simulations, the pedestal width is calculated by using the magnetic and flow shear stabilization model and the edge pressure gradient is limited by ballooning mode instability. The transport within the pedestal between ELM crashes is assumed to be only ion neoclassical. It is found that the simulations using the pressure gradient limited by MHD ballooning stability approximately reproduce the experimental data for the pressure profiles. A stability analysis indicates that an access to second stability in low triangulairty is closed by low-*n* kink/peeling modes while there is limited access to second stability region of ballooning modes in high triangularity discharges. For the high triangularity discharges, the pressure gradient is limited by finite-*n* ballooning modes. Since there is an access to second stability region of ballooning modes in the simulations of high triangularity discharges, the pedestal normalized pressure gradient in these discharges can achieve higher edge normalized pressure gradients than that achieved in low triangularity discharges.

ACKNOWLEDGEMENTS

The authors are grateful to Dr. A. Loarte, Dr. P. Monier-Garbet, Dr. G. Saibene and Dr. R. Sartori for their eorts in providing the experimental data that appears in this paper. One author (T. Onjun) thanks the Royal Thai Government and the Development and Promotion for Science and Technology Talents Project of Thailand (DPST) for their support. This work was conducted partly under European Fusion Development Agreement. It was supported in part by the U.S. Department of Energy (DOE) under contract No. DE-FG02-92-ER-5414, by the UK Department of Trade and Industry, and by EURATOM.

REFERENCES

[1]. G. Cennachi and A. Taroni, JET-IR(88) **03** (1988).

[2]. C. E. Singer, D. E. Post, D. R. Mikkelsen, et al., Computer Physics Communications **49**, 275 (1988).

[3]. T. Onjun, G. Bateman, A. H. Kritz, and D. Hannum, Phys. Plasmas **8**, 975 (2001).

[4]. D. Hannum, G. Bateman, J. Kinsey, et al., Phys. Plasmas **8**, 964 (2001).

[5]. J. Stober, O. Gruber, A. Kallenbach, et al., Plasma Physics and Controlled Fusion **42**, A211 (2000).

[6]. W. Suttrop, M. Kaufmann, H. J. de Blank, et al., Plasma Physics and Controlled Fusion **39**, 2051 (1997).

[7]. L. D. Horton, J. P. Christiansen, J. Lingertat, et al., Plasma Physics and Controlled Fusion **41**, B329 (1999).

[8]. A. M. Dimits, G. Bateman, M. A. Beer, et al., Phys. Plasmas **7**, 969 (2000).

[9]. R. Aymar et al., Plasma Phys. Control. Fusion **44**, 519 (2002).

[10]. D. Meade et al., Fusion Technology **39**, 336 (2001).

[11]. J. Kinsey, T. Onjun, G. Bateman, et al., Nucl. Fusion **43**, 1845(2003).
[12]. M. Sugihara, Y. Igitkhanov, G. Janeschitz, et al., Nucl. Fusion **40**, 1743 (2000).
[13]. T. Onjun, G. Bateman, A. H. Kritz, and G. Hammett, Phys. Plasmas **9**, 5018 (2002).
[14]. J. G. Cordey et al., Nucl. Fusion **43**, 670 (2003).
[15]. W. A. Houlberg, K. C. Shaing, S. P. Hirshman, and M. C. Zarnstor, Phys. Plasmas 4 , 3231 (1997).
[16]. T. Davydova, G. Bateman, A. H. Kritz, and A. Pankin, Phys. Plasmas **10**, 3614 (2003).
[17]. G. Saibeneet al., in Proceedings of the 28th EPS Conference of Controlled Fusion and Plasma Physics, Madeira, Portugal (2001).
[18]. ITER Physics Basis Document, Nucl. Fusion **39**, 2175 (1999).
[19]. J.S. Lonnroth, V. V. Parail, G. Corrigan, et al., Plasma Phys. Control. Fusion **45**, 1689 (2003).
[20]. M. Erba, A. Cherubini, V. V. Parail, et al., Plasma Physics and Controlled Fusion **39**, 261 (1997).
[21]. H. R. Wilson, J. W. Connor, A. R. Field, et al., Phys. Plasmas **6**, 1925 (1999).
[22]. P. Gohil, Phys. Rev. Letters **61**, 1603 (1988).
[23]. G. T. A. Huysmans et al., in Proceeding of the 22nd EPS Conference on Controlled Fusion and Plasma Phys. Part I **19**, 201 (1995).
[24]. J. W. Connor, H. R. Hastie, H. R. Wilson, and R. L. Miller, Phys. Plasmas **5**, 2687 (1998).
[25]. H. R. Wilson and R. L. Miller, Phys. Plasmas **6**, 873 (1999).
[26]. J. Manickam, Phys. Fluids **B4** (1992).
[27]. A. Taroni et al., Contrib. Plasma Phys **38** (1998).
[28]. V. Parail et al., in Proceeding of the 27th EPS Conference on Controlled Fusion and Plasma Phys. (2000).

.

Symbol	Units	Description
a	m	Plasma minor radius (half-width)
r	m	Flux surface minor radius (half-width)
R	m	Major radius to geometric
		Center of each flux surface
κ		Plasma elongation
δ		Plasma triangularity
B_T	Tesla	Vacuum toroidal magnetic field at R
I_p	MA	Toroidal plasma current
n_{ped}	m^{-3}	Pedestal density
T_{ped}	keV	Pedestal temperature
$\partial p/\partial r$	Pa/m	Pressure gradient
Δ	m	Pedestal width
ρ_i	m	Ion gyro radius
s		Magnetic shear
α		Normalised pressure gradient
α_c		Maximum normalised pressure gradient
$\nu*$		Normalized collisionality
A_H	AMU	Hydrogenic isotope mass
ρ		Toroidal flux co-ordinate

TABLE I: Notation used in this paper.

	Pulse No: 53186	Pulse No: 53187	Pulse No: 53298	Pulse No: 52308
R	2.91	2.92	3.01	2.99
α	0.94	0.92	0.89	0.90
κ	1.69	1.74	1.72	1.74
δ	0.25	0.32	0.45	0.49
B_T	2.61	2.61	2.68	2.69
I_p	2.50	2.50	2.49	2.50
A_H	2.00	2.00	2.00	2.00
Z_{eff}	2.03	2.03	2.59	1.60

TABLE II: List of discharges used in this paper

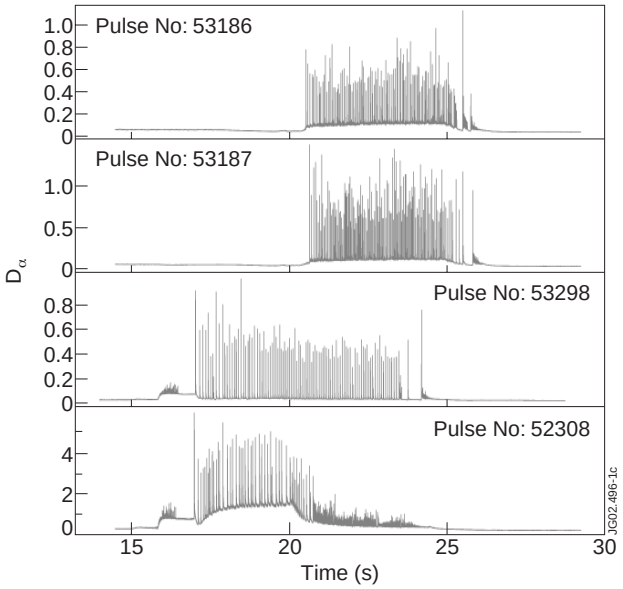

Figure 1: The time history of the D_α signal, measured at the edge of the plasma, is shown for JET Pulse No: 53186, 53187, 53298 and 52308.

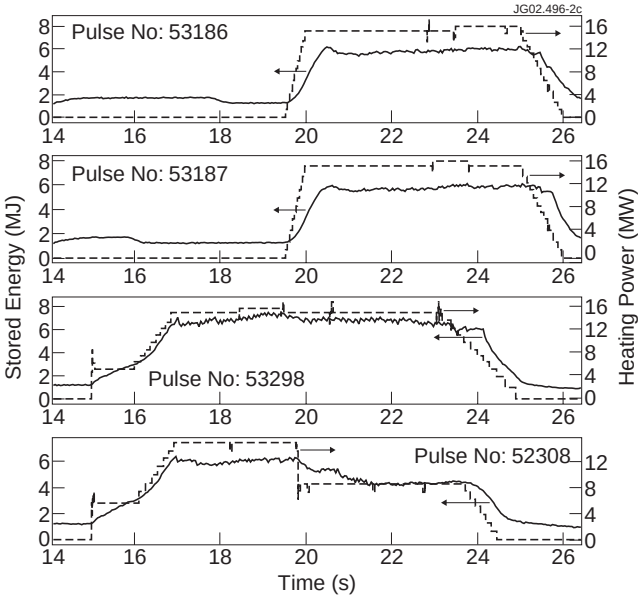

Figure 2: The time history of the stored plasma energy (solid lines) and that of the heating power (dashed lines) is plotted for JET Pulse No's: 53186 (top panel), 53187 (second panel), 53298 (third panel) and 52308 (bottom panel).

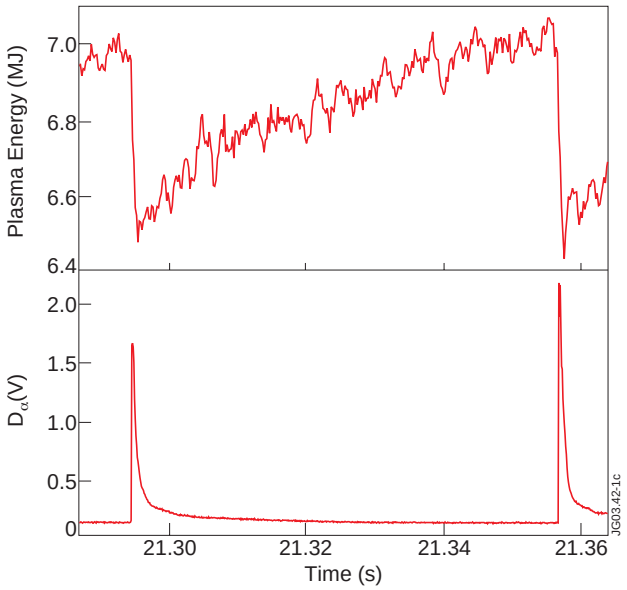

Figure 3: The measured stored plasma energy (top panel) and the D_α signal (bottom panel) are plotted as a function of time between two consecutive type I ELMs for Pulse No: 53298.

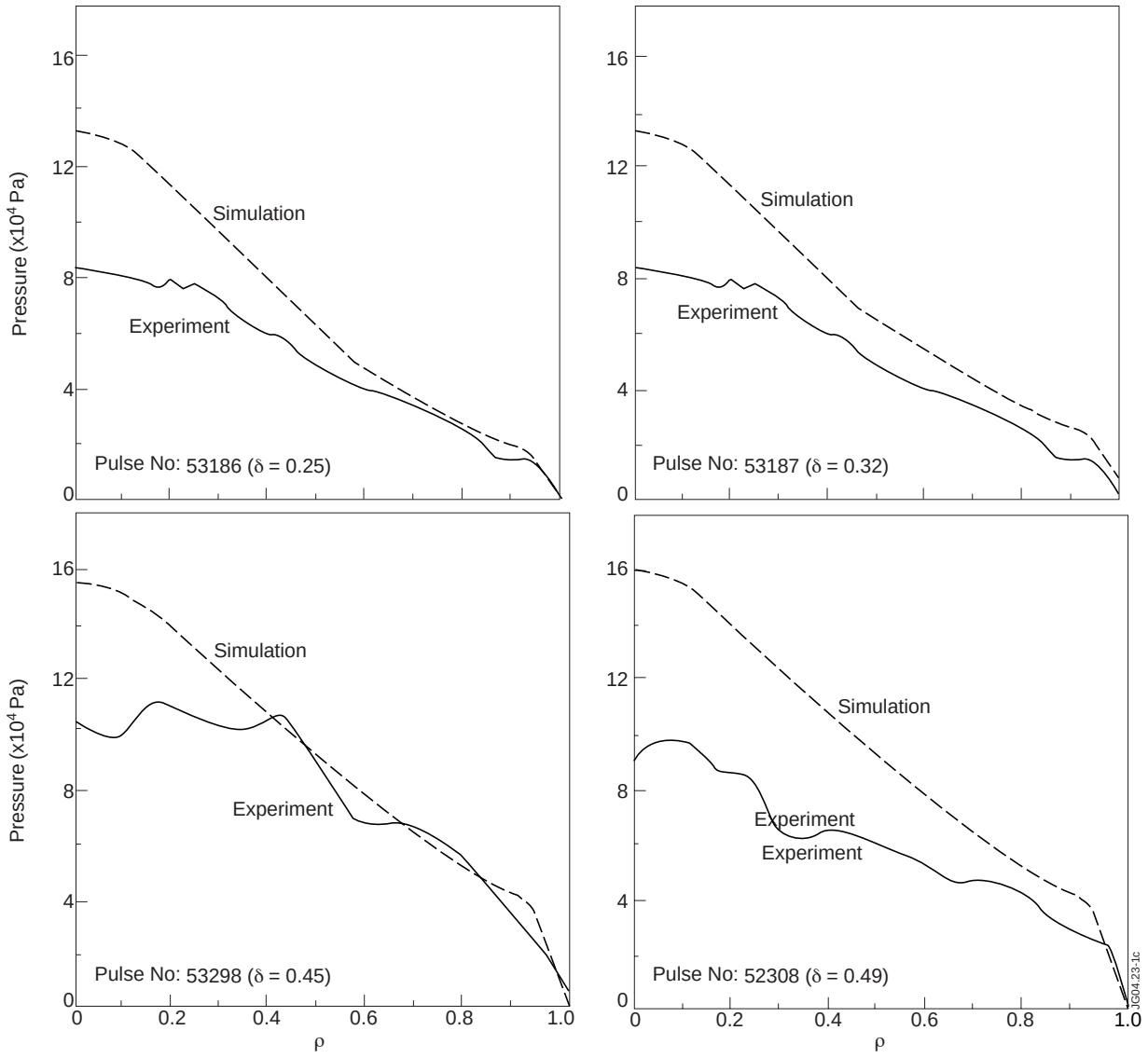

Figure 4: Predicted and experimental pressure are plotted as a function of normalized minor radius at a time just before an ELM crash for Pulse No's 53186, 53187, 53298 and 52308.

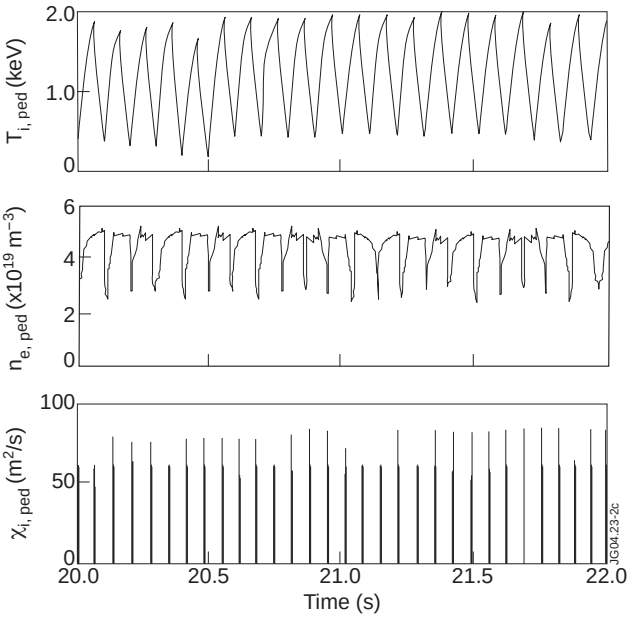

Figure 5: The ion temperature (top panel), electron density (middle panel) and ion diusivity (bottom panel) at the top of the pedestal are plotted as a function of time for Pulse No: 53298 (δ = 0.45).

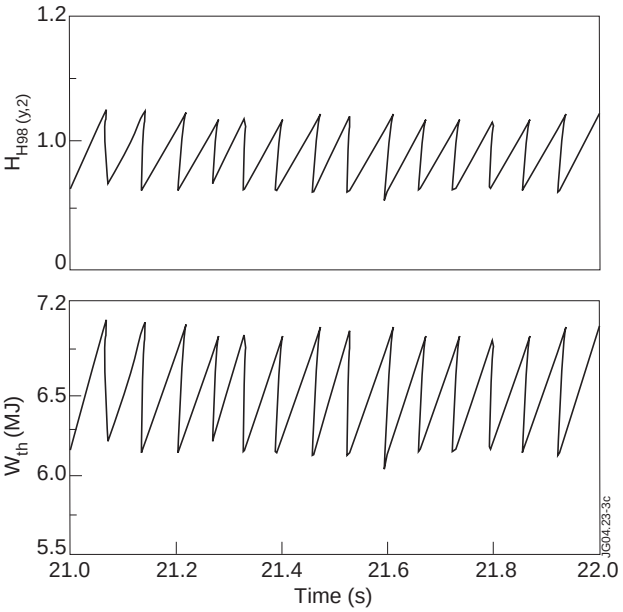

Figure 6: The $H_{H98(y;2)}$ factor and the stored energy (W_{th}) are plotted as a function of time for the JET Pulse No: 53298 (δ = 0.45). The $H_{H98(y;2)}$ factor is defined as $H_{H98(y;2)} \equiv \tau_{E;th} / \tau_{E;th}^{IPB98(y;2)}$, where $\tau_{E;th}$ is the thermal energy connement time.

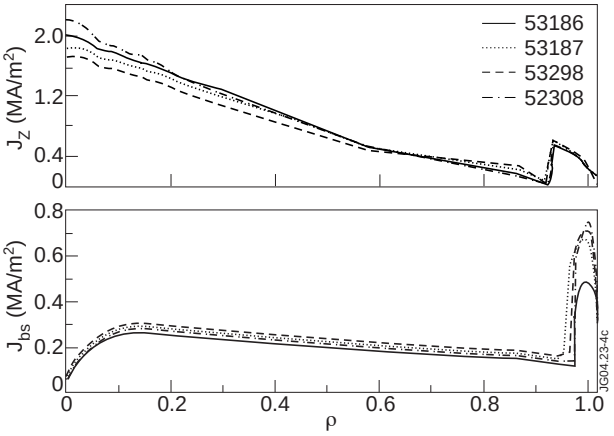

Figure 7: The simulated plasma current density, J_z, (top panel) and the bootstrap current density, J_{bs} (bottom panel) are plotted as a function of normalized minor radius, at a time just before an ELM crash, for JET Pulse No: 53186, 53187, 53298 and 52308.

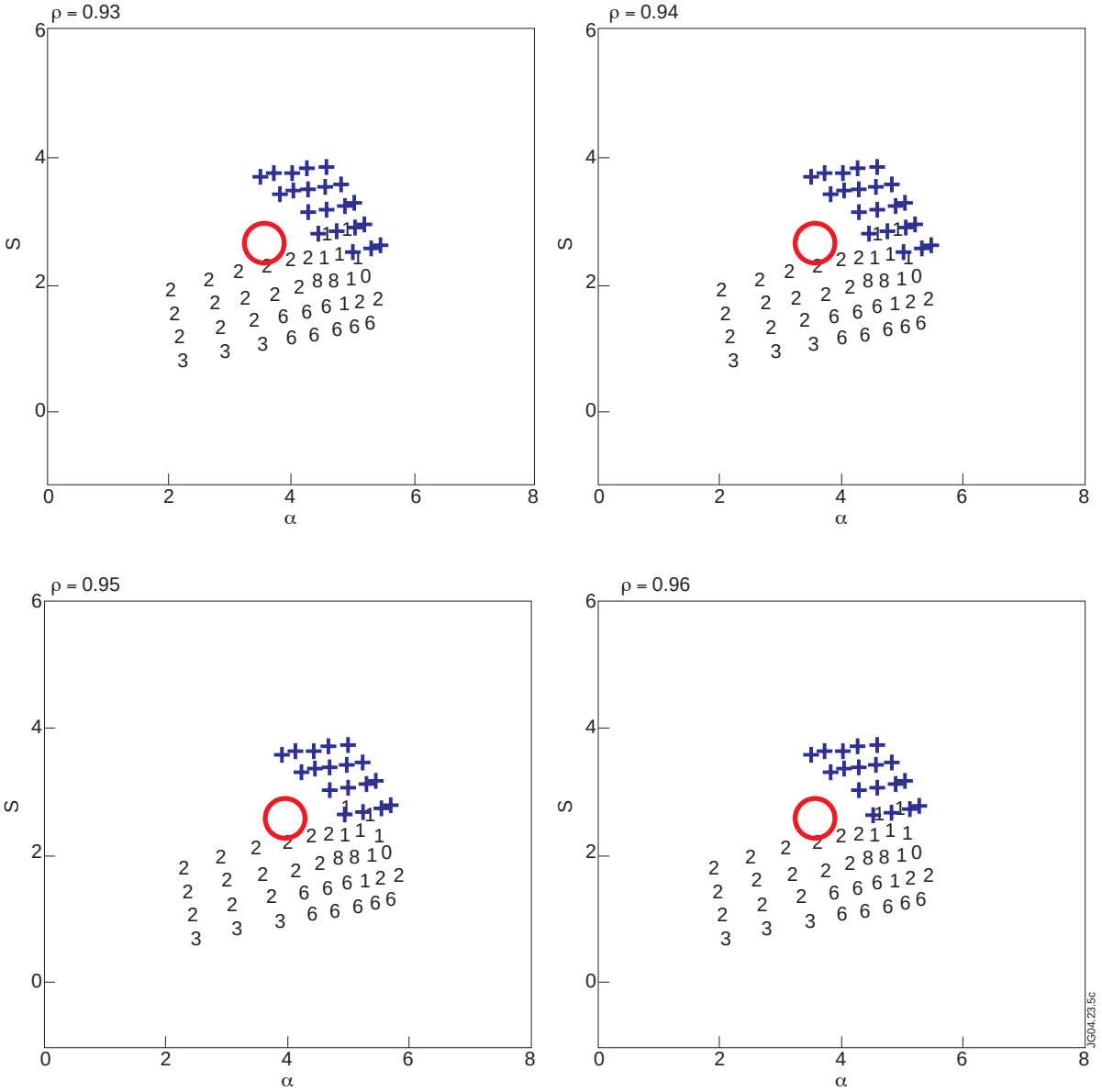

Figure 8: Stability results obtained using the HELENA and MISHKA codes are plotted for 93%, 94%, 95% and 96% flux surfaces on an s-α stability diagram for Pulse No: 53186 (δ = 0.25). The region of instability associated with the infinite-n ideal ballooning modes is indicated with crosses. The numbers indicate the most unstable finite-n ballooning and low-n kink/peeling modes at each location on the s-α plane. The region without numbers or crosses is the region where all modes are stable.

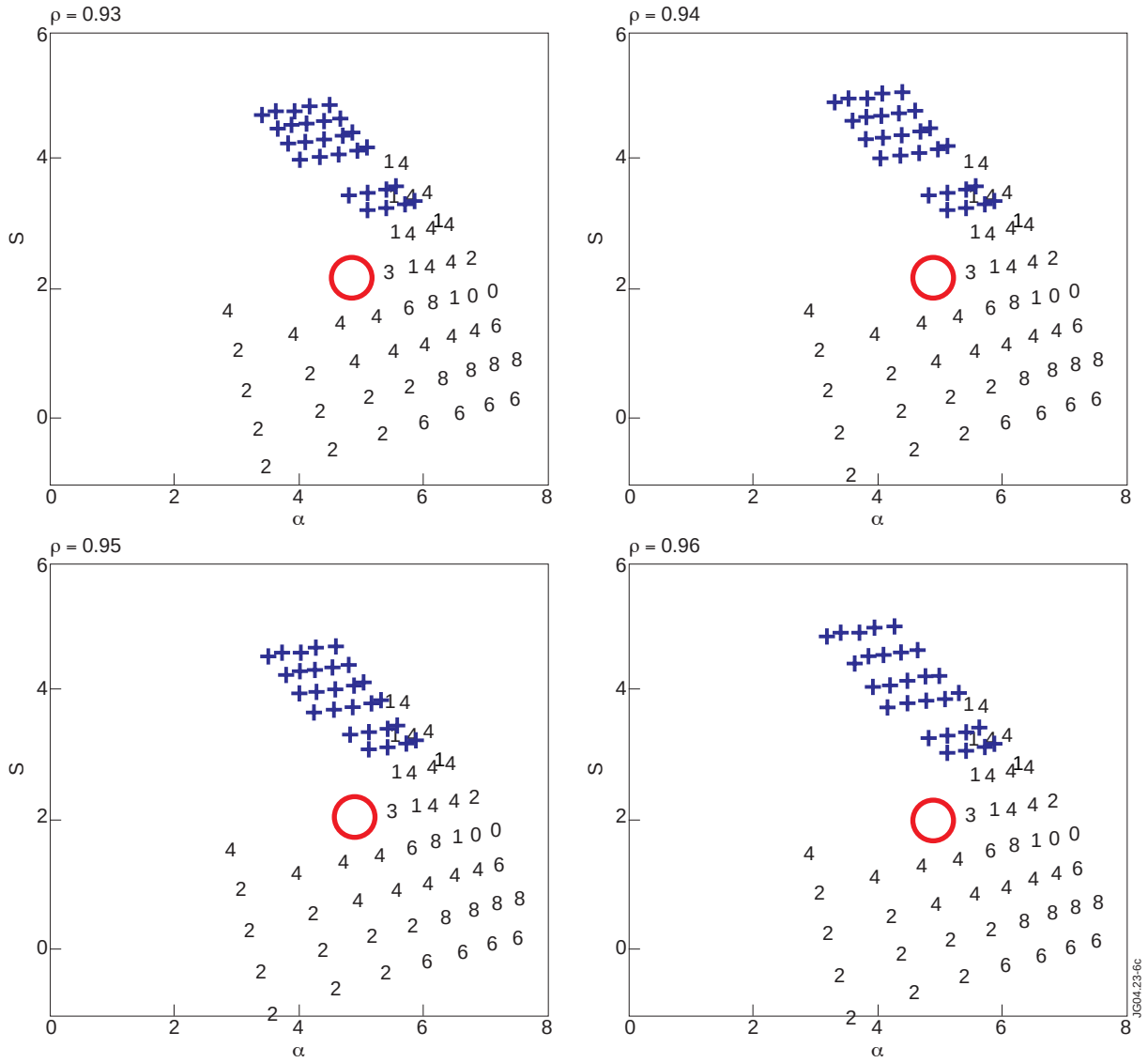

Figure 9: Stability results obtained using the HELENA and MISHKA codes are plotted for 93%, 94%, 95% and 96% flux surfaces on an s-α stability diagram for Pulse No: 53187 (δ = 0.32). The region of instability associated with the infinite-n ideal ballooning modes is indicated with crosses. The numbers indicate the most unstablenite-n ballooning and low-n kink/peeling modes at each location on the s-α plane. The region without numbers or crosses is the region where all modes are stable.

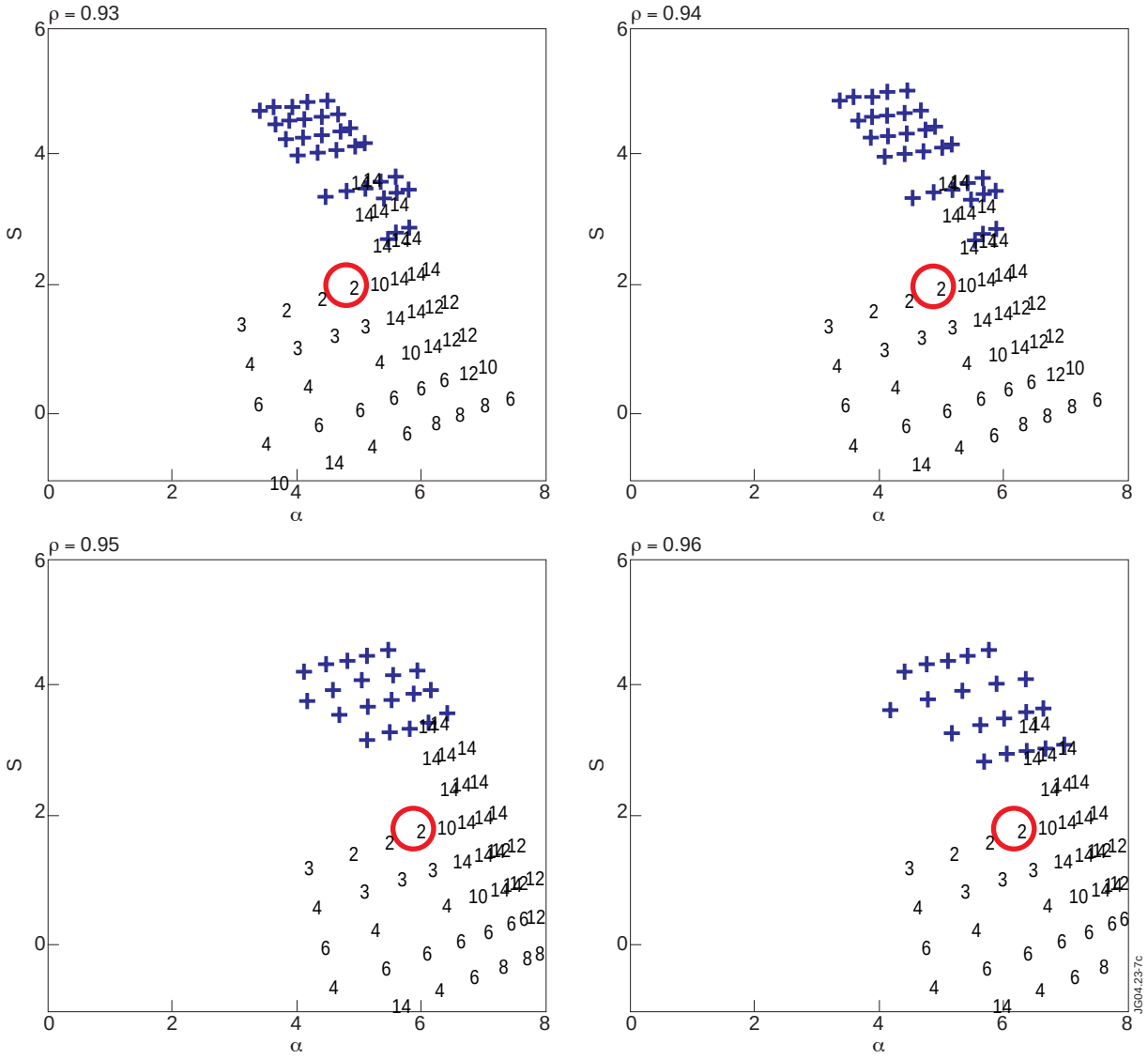

Figure 10: Stability results obtained using the HELENA and MISHKA codes are plotted for 93%, 94%, 95% and 96% flux surfaces on an s-α stability diagram for Pulse No: 53298 (δ = 0.45). The region of instability associated with the infinite-n ideal ballooning modes is indicated with crosses. The numbers indicate the most unstablenite-n ballooning and low-n kink/peeling modes at each location on the s-α plane. The region without numbers or crosses is the region where all modes are stable.

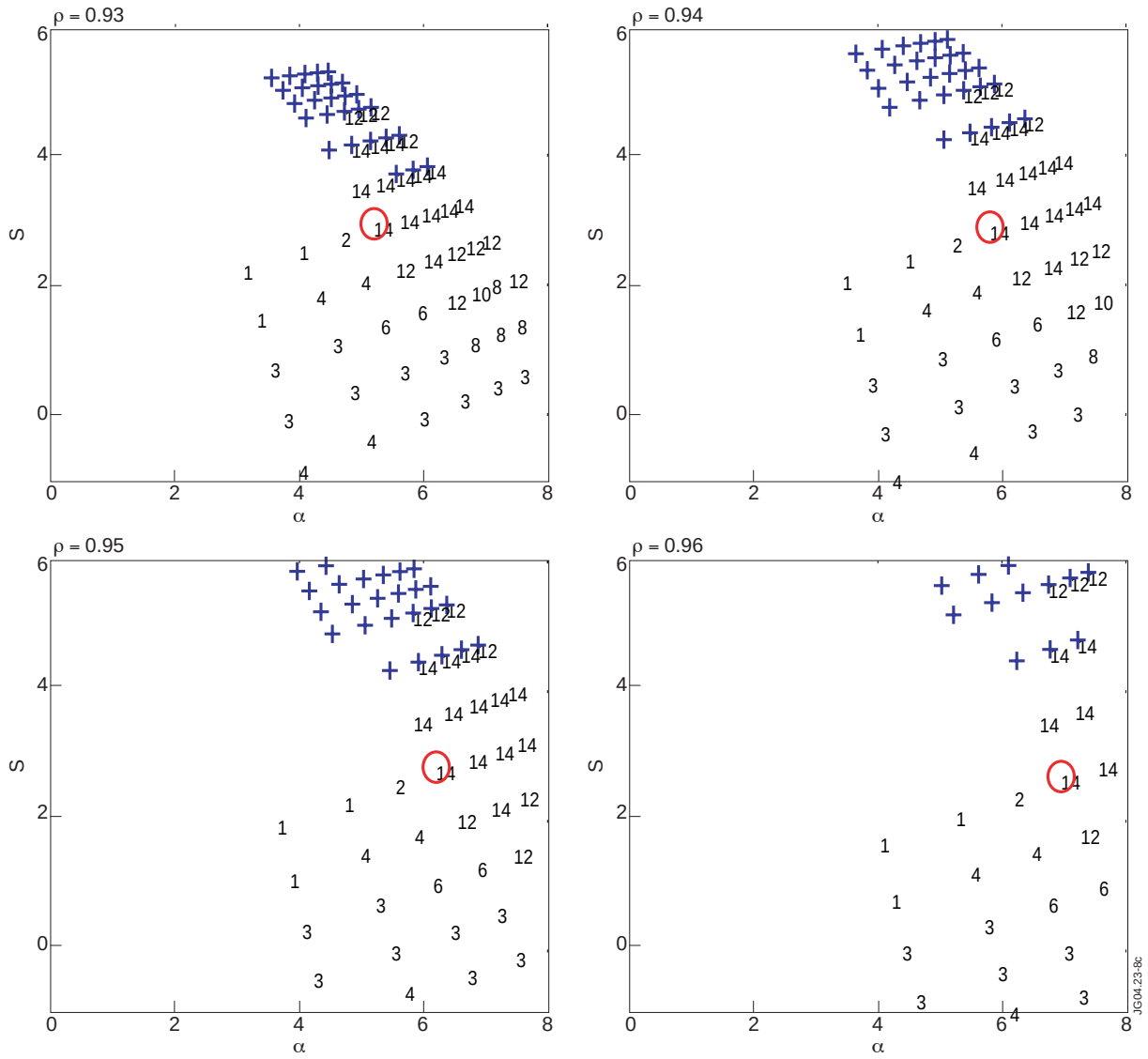

Figure 11: Stability results obtained using the HELENA and MISHKA codes are plotted for 93%, 94%, 95% and 96% flux surfaces on an s-α stability diagram for Pulse No: 52308 (δ = 0.49). The region of instability associated with the infinite-n ideal ballooning modes is indicated with crosses. The numbers indicate the most unstable finite-n ballooning and low-n kink/peeling modes at each location on the s-α plane. The region without numbers or crosses is the region where all modes are stable.